Intermixed Donor/Acceptor Region in Conjugated Polymer Blends Visualized by Conductive Atomic Force Microscopy

Miki Osaka, Hiroaki Benten,[#,] Hideo Ohkita, Shinzaburo Ito*

Department of Polymer Chemistry, Graduate School of Engineering, Kyoto University, Katsura, Nishikyo, Kyoto 615-8510, JAPAN

Present Address: [#]Graduate School of Materials Science, Nara Institute of Science and Technology, Takayama-cho, Ikoma, Nara 630-0192, JAPAN

ABSTRACT

The charge-transport characteristics of phase-separated blend films of poly(3-hexylthiophene) (P3HT; electron donor) and poly[2,7-(9,9-didodecylfluorene)-*alt*-5,5-(4′,7′-bis(2-thienyl)-2′,1′,3′-benzothiadiazole)] (PF12TBT; electron acceptor) were visualized by conductive atomic force microscopy (C-AFM). The C-AFM hole-current images clearly showed two phases—an electrically conductive region assigned to the P3HT-rich donor domain and a non-conductive region assigned to the PF12TBT-rich acceptor domain. The hole current in the conductive region was small compared with that of a neat P3HT film with similar thickness, indicating that the P3HT-rich domain contained a large fraction of PF12TBT as a minor component. Thermal annealing initially increased the hole current throughout the P3HT-rich domain because of reorganization of the P3HT chains from their as-cast configurations. Further annealing increased the hole current mainly in the middle of the P3HT-rich domain, but it decreased the hole current in the boundary areas close to the PF12TBT-rich domain owing to the presence of an intermixed region with a gradient of the P3HT/PF12TBT composition ratio. After annealing at temperatures above the glass-transition point of PF12TBT, the widths of the intermixed regions decreased to ~30 nm as phase separation proceeded with decomposition of the intermixed region. Such variations in the intermixed region, which were electrically resolved by the C-AFM, accounted for the temperature dependence of the photovoltaic properties of P3HT/PF12TBT blend solar cells.

INTRODUCTION

Blends of conjugated polymers have recently emerged as promising material candidates for plastic electronics such as light-emitting diodes and photovoltaics.[1–3] Blending of different polymers can create new materials with useful functions that cannot be derived from each constituent polymer alone. In particular, polymer-blend solar cells composed of two types of conjugated polymers, with one acting as an electron donor (for hole transport) and the other as an acceptor (for electron transport), have gained increasing attention as an inexpensive source of renewable energy owing to their production advantages based on low-cost printing processes and high throughput.[4–6]

The device functions of a blend film based on conjugated polymers are intrinsically dependent on the nanoscale blend morphology that varies with film processing conditions such as choice of the spin-coating solvent and inclusion of thermal annealing.[5,7–12] In particular, the morphological features of the donor/acceptor interface are of prime importance in polymer-blend solar cells because they are correlated to the efficiencies of charge generation, transport, and recombination, and thus overall device performance.[6,10,13–15] However, morphology optimization of polymer blends has long been conducted through trial and error because the relationship between the blend morphology and local electrical properties has not been fully established. Therefore, direct observation of these properties on the nanometer scale is critical for understanding how blend morphology affects device functions. Conductive atomic force microscopy (C-AFM) offers insights into these issues by providing high-resolution direct view of the local electrical properties of conjugated-polymer blends.[16–21]

In this article, we present the local electrical characteristics of conjugated-polymer blends based on a semicrystalline electron donor, poly(3-hexylthiophene) (P3HT), and an amorphous electron acceptor, poly[2,7-(9,9-didodecylfluorene)-*alt*-5,5-(4′,7′-bis(2-thienyl)-2′,1′,3′-benzothiadiazole)] (PF12TBT). In a previous study, we showed that thermal annealing plays

a crucial role in determining the device performance of P3HT/PF12TBT blend solar cells.[22] To obtain fine details of the electrical characteristics that are subject to change because of thermal annealing, we employed a conductive atomic force microscope equipped with a heating holder at the sample stage, which enabled us to obtain current images at the same location within a phase-separated nanostructure of the polymer blends. The evolving features of the intermixed donor/acceptor region that were electrically resolved by the C-AFM measurements accounted for the temperature dependence of the photovoltaic properties of P3HT/PF12TBT blend solar cells.

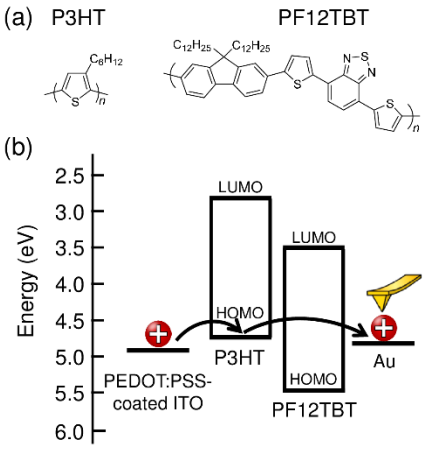

Figure 1. (a) Chemical structures of P3HT and PF12TBT. (b) Energy level diagram of PEDOT:PSS-coated ITO electrode, P3HT, PF12TBT, and Au electrode. Each energy level is taken from the literature: a work function of 4.9 eV for PEDOT:PSS|ITO,[23] 4.8 eV for Au;[24] the highest occupied molecular orbital (HOMO) energies of 5.5 eV for PF12TBT and 4.7 eV for P3HT; and the lowest unoccupied molecular orbital (LUMO) energies of 3.5 eV for PF12TBT and 2.7 eV for P3HT.[22]

EXPERIMENTAL

Materials. The donor polymer, regioregular P3HT, was purchased from Aldrich Chemical Co., USA (lot MKBD3325V). According to the Certificate of Analysis, the head-to-tail regioregularity, weight-average molecular weight (M_w), and polydispersity index (PDI, given

by M_w/M_n, where M_n is the number-average molecular weight) were 90.0%, 42300 g mol^{-1}, and 1.9, respectively. The amorphous acceptor polymer, PF12TBT, was synthesized and characterized by Sumitomo Chemical Co., Ltd., Japan: the values of M_w, PDI, and T_g were 20000 g mol^{-1}, 2.0, and 81 °C, respectively. The chemical structures of P3HT and PF12TBT are shown in Figure 1(a). Poly(3,4-ethylenedioxythiophene):poly(4-styrenesulfonate) (PEDOT:PSS) was purchased as PH-500 from H. C. Starck, USA.

Sample Preparation. Indium–tin-oxide (ITO) (flat ITO, GEOMATEC, Japan) substrates, glass substrates, and quartz substrates were ultrasonically washed with toluene, acetone, and ethanol in three 15-min sequences; the substrates were then dried with a N_2 flow. The cleaned substrates were further treated with an ultraviolet–ozone (UV–O_3) cleaner (NL-UV2535, Nippon Laser & Electronics Lab., Japan) for 30 min. An 80-nm-thick PEDOT:PSS layer was first spin-coated at 400 rpm for 10 s and then at 3000 rpm for 99 s onto each ITO substrate, after which it was dried in air at 140 °C for 30 min. Next, a P3HT/PF12TBT blend film was spin-coated from a solution of the blend in chlorobenzene (CB), at a spinning rate of 1500 rpm for 120 s, onto each PEDOT:PSS|ITO substrate and each glass substrate. The blend solution was prepared by mixing P3HT and PF12TBT at a weight ratio of 1:1 in CB, namely, 7.5 mg of P3HT and 7.5 mg of PF12TBT were dissolved in 1 mL of CB. A neat P3HT film was prepared by spin-coating a 10 mg mL^{-1} solution in chloroform at a spinning rate of 3000 rpm for 60 s onto the PEDOT:PSS|ITO substrate. The thickness of the P3HT/PF12TBT blend and neat P3HT films was measured by a contact-mode AFM (SPM-9600, Shimadzu, Japan) as follows: a part of each film was scratched with a sharp needle to expose the substrate, and the film thickness was evaluated from the difference in height between the film and substrate surface. The thickness of each P3HT/PF12TBT blend film was ~65 nm and that of the neat P3HT film was 50 nm.

Solar Cell Fabrication and Characterization. The solar-cell characteristics were measured

for each P3HT/PF12TBT blend film sandwiched by the PEDOT:PSS|ITO substrate and the Ca/Al electrode. The P3HT/PF12TBT blend films were spin-coated onto PEDOT:PSS|ITO substrates; each film was then annealed at a different temperature (60, 80, 100, 120, or 140 °C) for 10 min under a N_2 atmosphere. Finally, a calcium interlayer (thickness: 10 nm) and an aluminum electrode (thickness: 70 nm) were sequentially vacuum-deposited at 2.5×10^{-4} Pa through a shadow mask. The active area of each device, defined as the area of the top Ca/Al electrode, was 0.07 cm^2. The current-density–voltage (*J*–*V*) characteristics were measured by using a direct-current voltage and a current source monitor (R6243, Advantest, Japan) under illumination by an AM1.5G simulated solar light with a power density of 100 mW cm^{-2} at 21 °C.

C-AFM Measurements. The P3HT/PF12TBT blend films were prepared on PEDOT:PSS|ITO substrates and annealed separately at different temperatures (60, 80, 100, 120 or 140 °C) for 10 min in a N_2 atmosphere. Conductive-AFM measurements were performed using the microscope (SPM-9600, Shimadzu, Japan) in contact mode. In these measurements, Au-coated silicon probes (PPP-CONTAu, NANOSENSORS, Switzerland; tip radius: <50 nm; spring constant: 0.2–0.25 N m^{-1}) were used to ensure that holes were the major carriers of the current.[21,25] A sample bias was applied to the ITO substrate, and the probe was grounded. The surface topography and corresponding current images were simultaneously obtained by the C-AFM operating at a constant sample bias of +3.0 V. All C-AFM measurements were performed under a N_2 atmosphere in a controlled-environment chamber (CH-III, Shimadzu, Japan). The energy level diagram of the electrodes and polymers is shown in Figure 1b.

C-AFM Fixed-Point Measurements. Figures 2a and 2b show an illustration of the setup and the operating procedure, respectively, of the C-AFM measurements at a fixed position.[26] The sample was heated by using the sample heating unit (Shimadzu, Japan), as shown in Figure 2a. First, the as-cast (non-annealed) P3HT/PF12TBT blend film was measured. After the probe

was released from the surface, the film was thermally annealed at 80 °C for 10 min by the heating unit under the sample. After the annealed film was cooled to room temperature, the probe was placed again on the film surface in the same region for the measurement before annealing, and the surface topology and a current image were obtained. Next, the film was annealed again at 80 °C for 50 min and images were obtained in the same manner after cooling. These annealing and measurement cycles were carried out under a N_2 atmosphere.

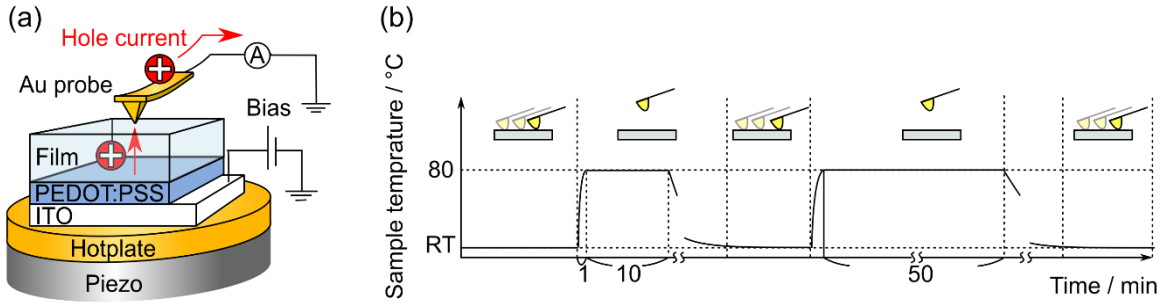

Figure 2. (a) Illustration of the conductive atomic force microscope (C-AFM) employed in this study.[26] A hot plate was located between the sample and the piezoelectric element. Sample bias was applied to the ITO substrate, and the probe was grounded. (b) Operating procedure of C-AFM measurements at a fixed position. The measurements were obtained at room temperature (RT), and the sample was annealed at 80 °C by the underlying hot plate after the probe was released from the sample surface.

Absorption Measurements. After the films were thermally annealed at 80 °C for 10 min and 60 min under a N_2 atmosphere, the UV–visible (UV–vis) absorption spectra (U-3500, Hitachi, Japan) of P3HT/PF12TBT blend films prepared on glass substrates were measured at room temperature.

Photoluminescence Quenching Measurements. Using a calibrated fluorescence spectrophotometer (Hitachi, F-4500, Japan), photoluminescence (PL) spectra were measured for the as-cast neat PF12TBT film and P3HT/PF12TBT blend films that were as-cast and annealed at a different temperature (60, 80, 100, 120, or 140 °C) for 10 min in a N_2 atmosphere.

The neat and blend films used for the PL measurement were spin-coated on quartz substrates. The excitation wavelength was set at 392 nm to excite mostly the PF12TBT component (the excitation fraction of PF12TBT was 75%, while that of P3HT was 25%). The PL intensity was corrected for variations in the PF12TBT absorption at 392 nm. The PL quenching efficiency (Φ_q) of PF12TBT in the blend film was evaluated from the ratio of the PL intensity of the P3HT/PF12TBT blend films to that of the as-cast neat PF12TBT film.

RESULTS

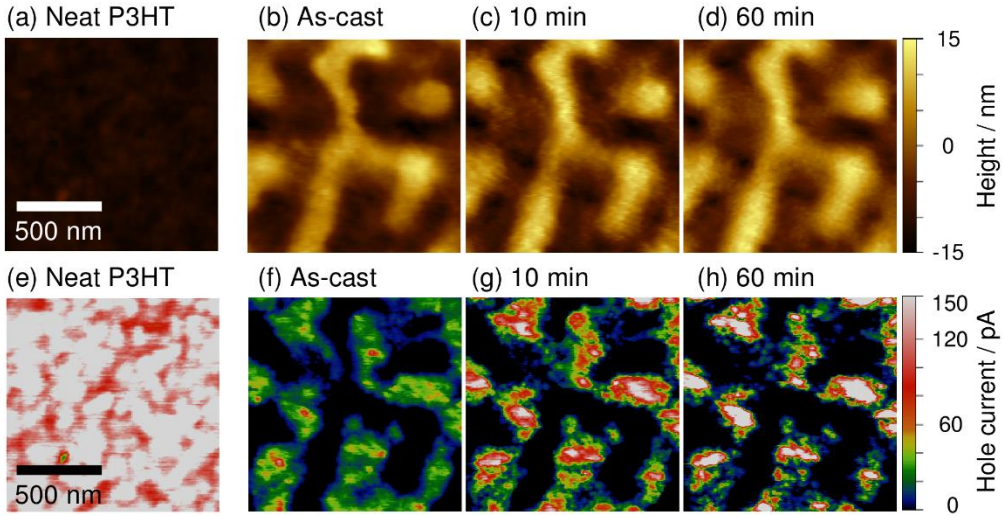

Figure 3. (a) Topographical and (e) hole-current images (1.25 × 1.25 μm^2) of an as-cast neat P3HT film. (b–d) Topographical and (f–h) hole-current images (1.25 × 1.25 μm^2) of a P3HT/PF12TBT blend film. These images were obtained from the same area of the blend film that was (b, f) as-cast and one that was annealed at 80 °C sequentially for (c, g) 10 min and then for (d, h) 50 min (total annealing duration: 60 min).

Thermal Annealing of a Blend Film at T_g of PF12TBT. *C-AFM Current Images*. Figure 3 shows C-AFM topographical images and the corresponding hole-current images of an as-cast neat P3HT film and a P3HT/PF12TBT blend film that was as-cast, annealed at 80 °C for 10 min, and further annealed for 50 min (total annealing duration: 60 min). The C-AFM images

were obtained in the same area of the blend film before and after annealing. The spatially inhomogeneous current distribution in the as-cast neat P3HT film, with relatively low conductive regions and high conductive domains, was attributed to the regions of relatively low and high density of P3HT nanocrystallites in the film as previously reported.[25,26] The topographical images of the blend film show distinct phase-separated structures consisting of connected domains. On the other hand, the hole-current images of the blend film clearly show two phases: an electrically conductive region and a non-conductive region. The hole current was detected selectively from the lower region of the topographical image (cross-sectional profiles of the height and current flow are provided in Supporting Information, Figure S1). The hole current observed in the as-cast blend film was spatially inhomogeneous and significantly smaller than that in the neat P3HT film. It should be noted that the thickness of the neat P3HT film was adjusted to be 50 nm, which is the same as that of the conductive region in the blend film. After thermal annealing at the glass-transition temperature (T_g) of PF12TBT (T_g = 81 °C), the hole current increased but remained below that of the neat P3HT film. The increase in the hole current suggests that morphological changes took place in the as-cast blend film, despite not being observable in the topographical images in Figure 3.

Figure 4 shows histograms of the current observed at each pixel in the image of the as-cast neat P3HT film (Figure 3e) and in the conductive region in the P3HT/PF12TBT blend film before and after thermal annealing for 10 min (Figures 3f and 3g). As shown in the histograms, the current values were less than 70 pA for the as-cast blend film, while they were over 70 pA for the neat P3HT film. On the other hand, the current had widely distributed values, including some above 70 pA, after annealing, revealing that the improved local hole conductivity was comparable to that of the as-cast neat P3HT film.

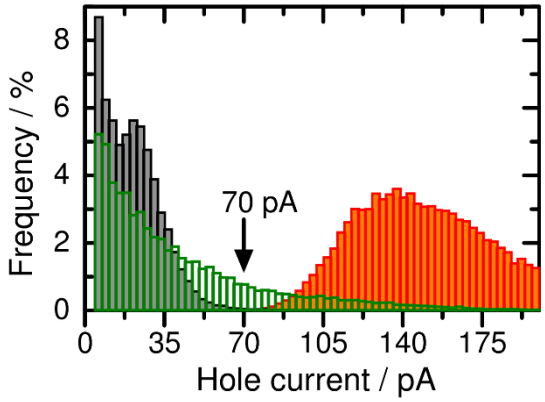

Figure 4. Histograms of the hole current observed at each pixel in the image of the conductive region in the P3HT/PF12TBT blend film that was as-cast (black solid lines, Figure 3f) and annealed at 80 °C for 10 min (green solid lines, Figure 3g). The red bars represent the histogram of current values of the as-cast neat P3HT film shown in Figure 3e.

To examine how thermal annealing affected local hole transport in the P3HT/PF12TBT blend film, we calculated the change in the local hole current, ΔI, at each pixel due to thermal annealing at 80 °C for a certain period. Figure 5a shows ΔI mapping images of the blend film before and after thermal annealing for 10 min; the black lines represent the border between the conductive (colored) and non-conductive (black) regions observed in the as-cast blend film (Figure 3f). Figure 5b shows ΔI mapping images of the blend film before and after additional thermal annealing for 50 min; the black lines represent the border between the conductive (colored) and non-conductive (black) regions observed in the blend film that was annealed for 10 min (Figure 3g). In these images, the red, green, and white regions represent parts of the films in which $\Delta I > 0$, $\Delta I < 0$, and $\Delta I = 0$, respectively. During the first 10 min of annealing, the local hole current increased for the most part within the conductive region in the as-cast blend film (Figure 5a). During the additional 50 min of annealing, the local hole current further increased in the middle of the conductive region, but it decreased on the side close to the border with the non-conductive region.

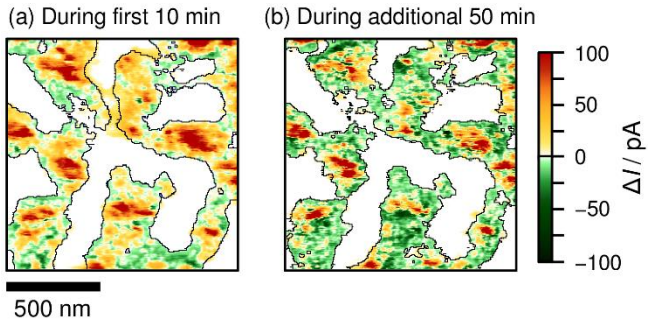

Figure 5. (a) Mapping of ΔI caused by the first 10 min of annealing at 80 °C. (b) Mapping of ΔI caused by the following 50 min of annealing at 80 °C. The black lines overlaid in each image represent the border between conductive and non-conductive regions defined in the (a) as-cast P3HT/PF12TBT blend film (Figure 3f) and (b) P3HT/PF12TBT blend film that was annealed at 80 °C for 10 min (Figure 3g).

Absorption Spectra. Figure 6 shows the absorption spectra of the blend films. The absorption intensity at around 600 nm increased after the first 10 min of annealing, but it barely changed after the following 50 min of annealing. These findings suggest that the ordering of P3HT chains proceeded mostly during the first 10 min.

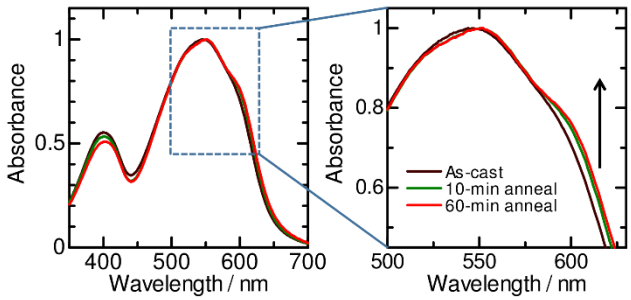

Figure 6. UV–vis absorption spectra of the P3HT/PF12TBT blend film: as-cast (black line); annealed at 80 °C for 10 min (green line); further annealed for 50 min (red line).

Thermal Annealing of Blend Films at Temperatures Above and Below T_g of PF12TBT.

C-AFM Current Images. We annealed the blend film at different temperatures above and

below the glass-transition point of PF12TBT (T_g = 81 °C). Figure 7 shows C-AFM topographical and hole-current images of P3HT/PF12TBT blend films that were as-cast and annealed separately for 10 min at temperatures of 60, 80, 100, or 140 °C. The connected domain structures in the topographical image of the as-cast blend film remained after annealing at <80 °C, but the structures swelled and appeared fuzzy after annealing at 100 and 140 °C. The changes in the topographical images indicates that phase separation in the P3HT/PF12TBT blend was accelerated when the annealing temperature was above T_g of PF12TBT. On the other hand, the C-AFM current images show that the current value in the conductive region increased and the non-conductive region became larger after annealing at 100 and 140 °C. From the topographical images of the blend films, we calculated the autocorrelation functions (see the Supporting Information, Figure S2).[27] The correlation length and pseudoperiod of the dumped oscillation were found to be 106 and nearly 400 nm, respectively, for the as-cast blend film and 127 and nearly 600 nm, respectively, for the blend film annealed at 140 °C.

PL Quantum Efficiency and Device Performance. The PL quantum efficiency (PLQE) of PF12TBT in the P3HT/PF12TBT blend films relative to that of a neat PF12TBT film was calculated using the equation PLQE = 35.1 × (1 – Φ_q/100). The value of PLQE of the neat PFTBT film was assumed to be 35.1%, which is the value reported for the neat film of poly[9,9-dioctylfluorene-2,7-diyl-*alt*-[4,7-bis(3-hexylthiophen-5-yl)-2,1,3-benzothiadiazole]-2′,2′′-diyl] (F8TBT) by McNeill *et al*.[28] Figure 8a shows PLQE values of PF12TBT in the P3HT/PF12TBT blend films that were as-cast and annealed separately for 10 min at temperatures from 60 to 140 °C. The value of PLQE was in the range of 12–14% (Φ_q = 61–65%) for the as-cast blend film and the blend films annealed at 60 and 80 ºC, but it increased to 16% (Φ_q = 54%) for the blend film annealed at 100 °C and finally reached 20% (Φ_q = 44%) for the blend film annealed at 140 °C. Figure 8b shows the dependence of the short-circuit current density (J_{SC}) and fill factor (FF) of these blend films on the annealing temperature.

The value of J_{SC} increased from that of the as-cast blend film to the maximum value of films annealed at 60 and 80 °C; however, J_{SC} dropped drastically when the blend film was annealed at 100 °C, and then decreased slightly when the blend film was annealed at temperatures above 100 °C. On the other hand, the value of FF gradually increased with temperature up to 80 °C, sharply increased at 100 °C, and then slightly increased when the temperature was above 100 °C.

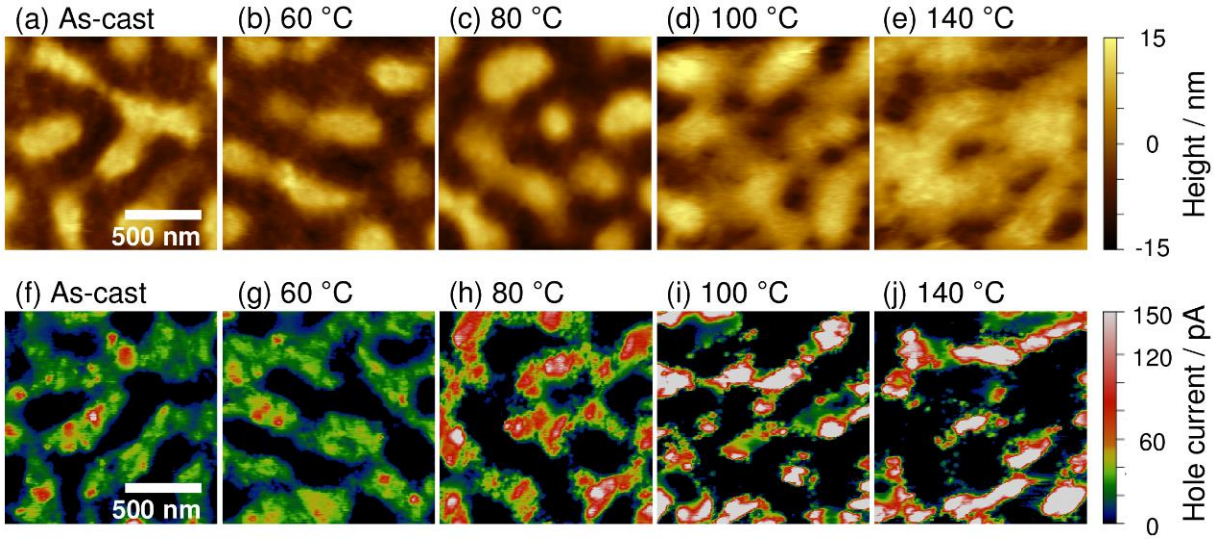

Figure 7. C-AFM (a–e) topographical and (f–j) hole-current images (1.25 × 1.25 μm^2) of P3HT/PF12TBT blend films that were (a, f) as-cast and annealed for 10 min at (b, g) 60 °C, (c, h) 80 °C, (d, i) 100 °C, and (e, j) 140 °C.

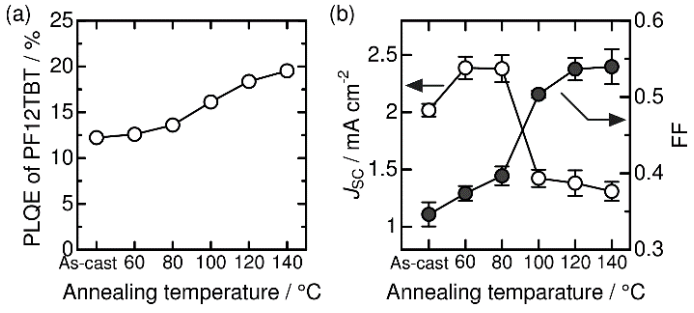

Figure 8. Dependence of the (a) PL quantum efficiency (PLQE) of PF12TBT, (b) short-circuit current density (J_{SC}, open circles) and fill factor (FF, solid circles) on the annealing temperature of the P3HT/PF12TBT blend films. The PLQE of the neat PF12TBT film was assumed to be 35.1%.[28]

DISCUSSION

Assignment of Domains. Since both hole and electron injections into the HOMO and LUMO of PF12TBT were difficult owing to the large energy barrier between the work functions of the electrodes and the HOMO and LUMO of PF12TBT, our C-AFM setup selectively detected the hole current through the HOMO of P3HT (see the Supporting Information, Figure S3).[21] We therefore assigned the topographically lower and conductive region (I > 0 pA) in the current images (Figures 3 and 7) to the P3HT-rich domain and the topographically higher and non-conductive region (I = 0 pA) to the PF12TBT rich-domain. For the as-cast blend film, the P3HT-rich domain contained PF12TBT as a minor component because the hole current was much smaller than that observed for the neat P3HT film. Similarly, the PF12TBT-rich domain was probably not pure and contained P3HT as a minor component. Utilizing near-field scanning photocurrent microscopy[29] and X-ray microscopy[30–32], McNeill and coworkers discovered the presence of a nanoscale intermixed morphology within micrometer-sized phase-separated domains of conjugated polymer blend films. After thermal annealing, the hole current in the P3HT-rich domain increased locally to >70 pA (Figure 4), which is comparable to that of the as-cast neat P3HT film. This highly conductive region (I > 70 pA) was assigned to the neat P3HT-like domain. On the other hand, the intermediate conductive region (0 < I < 70 pA) was assigned to an intermixed region of P3HT and PF12TBT. The domain assignment based on the local current values obtained by C-AFM is illustrated in Figure 9. It should be noted that the contrast in the surface potential image of the blend film (see the Supporting Information, Figure S4) is consistent with that in the topographic image. This finding shows that there is no capping layer of P3HT or PF12TBT on the surface of the blend films.

Nanoscale Morphology Leading to the Improvement in Hole Transport. In thin films of polymer/polymer blends prepared by spin-coating, the de-mixing process of the constituent

polymers remains far from a thermodynamically stable stage.[33] In such films, the constituent polymer chains are in constrained structures, and each polymer phase contains an excess amount of the other polymer.[7,29–32] As mentioned earlier, the changes in ΔI mapping images and absorption spectra resulting from the first 10 min of annealing at 80 °C are different from the changes resulting from the following 50 min of annealing at 80 °C, suggesting that there were two characteristic steps of improvement in hole transport in the blend film. During the first round of annealing, the local current increased in most parts within the P3HT-rich domain and was accompanied by an increase in the absorption intensity at 600 nm. During the following round of annealing, the local current further increased in the middle of the P3HT-rich domain, but it decreased at the interface close to the PF12TBT-rich domain, without an accompanying change in the absorption intensity. This initial spectral change indicates that the ordering of P3HT chains at 80 °C was completed during the first 10 min of annealing.[34–36] In this initial step, the as-cast P3HT chains relaxed from the constrained conformations to more ordered ones that were favorable for efficient hole transport. In the following step, the location-dependent change in the local current was associated with the compositional change within the P3HT-rich domain. As discussed in the following section, the morphological change was driven by the presence of an intermixed region with a gradient of the ratio between the P3HT and PF12TBT content.

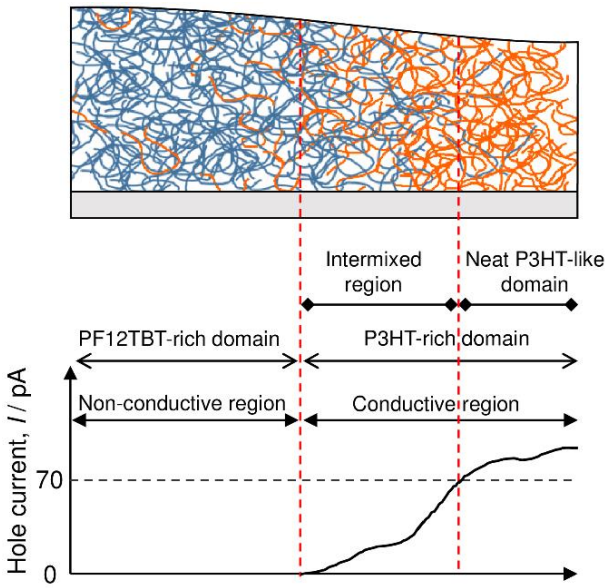

Figure 9. Illustration of the domain assignments in the P3HT/PF12TBT blend film. Depending on the value of the hole current (*I*) obtained by C-AFM, the conductive region in the blend film was divided into two areas: each area was classified as either an intermixed region ($0 < I < 70$ pA) or a neat P3HT-like domain ($I > 70$ pA). The non-conductive region ($I = 0$) was assigned to the PF12TBT-rich domain.

Intermixed Region in the Blend Films. *Location of the Intermixed Region.* To specify the location of the intermixed region, neat P3HT-like domain, and PF12TBT-rich domain in each blend film, we recolored the C-AFM current images in Figure 7 as follows: blue was used for the PF12TBT-rich domain with $I = 0$, purple was used for the intermixed P3HT/PF12TBT region with $0 < I < 70$ pA, and red was used for the neat P3HT-like domain with $I > 70$ pA. The recolored current images shown in Figure 10 indicate that (1) the size of the neat P3HT-like domain grew in the middle of the intermixed region and (2) the intermixed region was located in the area between the PF12TBT-rich and neat P3HT-like domains as it was consumed by these two expanding domains. In addition, the area occupancy of each domain varied as a function of the annealing temperature. The PF12TBT-rich domain occupied 32% of the as-cast blend film, and the occupancy increased to 50% in the blend film annealed at 140 °C. On

the other hand, the neat P3HT-like domain occupied as little as 1% of the as-cast blend film, and the occupancy increased to 20% of the blend film annealed at 140 °C. Consequently, the area occupied by the intermixed region decreased from 67% in the as-cast blend film to 30% in the blend film annealed at 140 °C. The increase in the current after annealing at a temperature above T_g is ascribed mainly to the compositional change in the intermixed region due to phase separation. In addition, the absorption spectra of the blend films showed apparent shoulder structures in the wavelength range of 500–650 nm after the annealing (see the Supporting Information, Figure S5), suggesting that ordering (or crystallization) of the P3HT chains also caused an increase in the current.

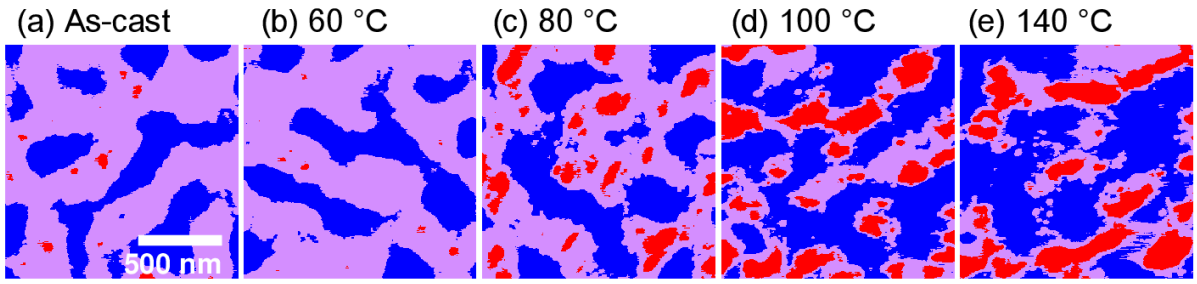

Figure 10. Distribution maps of areas of the PF12TBT-rich domain (blue), intermixed P3HT/PF12TBT region (purple), and neat P3HT-like domain (red) in each annealed P3HT/PF12TBT blend film. Each film was annealed for 10 min at a different temperature. These images were obtained by recoloring the current images in Figures 7f–7j.

Composition Gradients across P3HT-Rich Domain. To examine the composition gradient, we analyzed the current in the P3HT-rich domain as a function of the distance from the boundary of the PF12TBT-rich domain. An example of our analysis is shown in Figures 11a and 11b, and the analysis results are summarized in Figure 11c. Figure 11a is an enlarged view of the current image of the P3HT/PF12TBT blend film: it consists of pixels represented by squares measuring 4.9 × 4.9 nm^2. The local current I at each pixel was determined from this magnified current image of the P3HT-rich domain. On the other hand, the distance d

between the pixel in the P3HT-rich domain and the boundary of the PF12TBT-rich domain was determined as follows. First, the pixels on the boundary of the PF12TBT-rich domain were marked by the white circles, as shown in Figure 11a. Next, for all the pixels in the P3HT-rich domain, the distance d from the nearest pixel on the boundary was calculated. The value of d was then rounded to the nearest multiple of a, where a is a length of one pixel (i.e., 4.9 nm). In Figure 11b, we recolored all the pixels in the P3HT-rich domain according to the distance d, which varied from a to $6a$ and $>6a$. Finally, we averaged the local current at every pixel located at the same distance $d = na$, obtaining the value $I(d)$. As shown in Figure 11c, $I(d)$ increased with an increase in d for the as-cast blend film, indicating the presence of a gradient of the P3HT/PF12TBT composition across the P3HT-rich domain. Such composition gradient drove the phase separation that proceeded with consumption of the intermixed region between the PF12TBT-rich and neat P3HT-like domains.[37] Furthermore, the increase in the slope of $I(d)$ is an indication that the composition gradient became steep because of the progression of the phase separation.

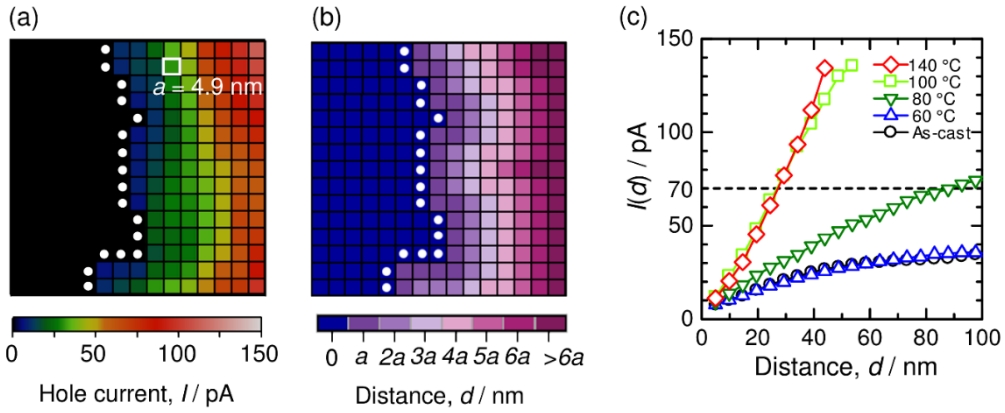

Figure 11. (a) Enlarged view of a current image of the P3HT/PF12TBT blend film. The current image consists of pixels with a size of 4.9 × 4.9 nm^2 (a set of 256 × 256 data points per 1.25 μm^2). (b) The P3HT-rich domain was recolored according to the distance d from the nearest boundary point of the PF12TBT-rich domain (white circles). (c) Correlation of $I(d)$ with the distance d from the boundary of the PF12TBT-rich domain. The broken line represents I = 70 pA.

Width of the Intermixed Region. We next evaluated the width of the intermixed region. The broken line in Figure 11c represents I = 70 pA, which was the threshold current separating the intermixed region ($0 < I < 70$ pA) and the neat P3HT-like domain ($I > 70$ pA). For the blend film annealed at 80 °C, $I(d)$ increased and approached 70 pA asymptotically at d = 80 nm. For the blend films annealed at 100 and 140 °C, $I(d)$ reached 70 pA at d = 30 nm. In other words, the width of the intermixed region decreased on average from 80 nm in the blend film annealed at 80 °C to 30 nm in the blend films annealed at 100 and 140 °C, as illustrated in Figure 12.

In order to determine the composition in the PF12TBT-rich domain, we examined the relationship between the area occupied by the PF12TBT-rich domain and PLQE of PF12TBT in the blend films. The black circles in Figure 13 represent the PLQE values plotted against the respective area occupancy of the PF12TBT-rich domain in each blend film after annealing at a different temperature. The broken line represents the expected values of PLQE under the assumption that PL of PF12TBT was quenched in the P3HT-rich domain but not in the PF12TBT-rich domain. As shown in this figure, the experimental PLQE values were larger than those represented by the broken line. Such deviation indicates that a part of the PL of PF12TBT was quenched even in the PF12TBT-rich domain because, just as we speculated, PF12TBT was mixed with the minor component, P3HT, in this region. Our results demonstrate that C-AFM current images can reveal fine details, with a resolution of tens of nanometers, of morphological features of the interface between donor and acceptor domains in polymer blends.

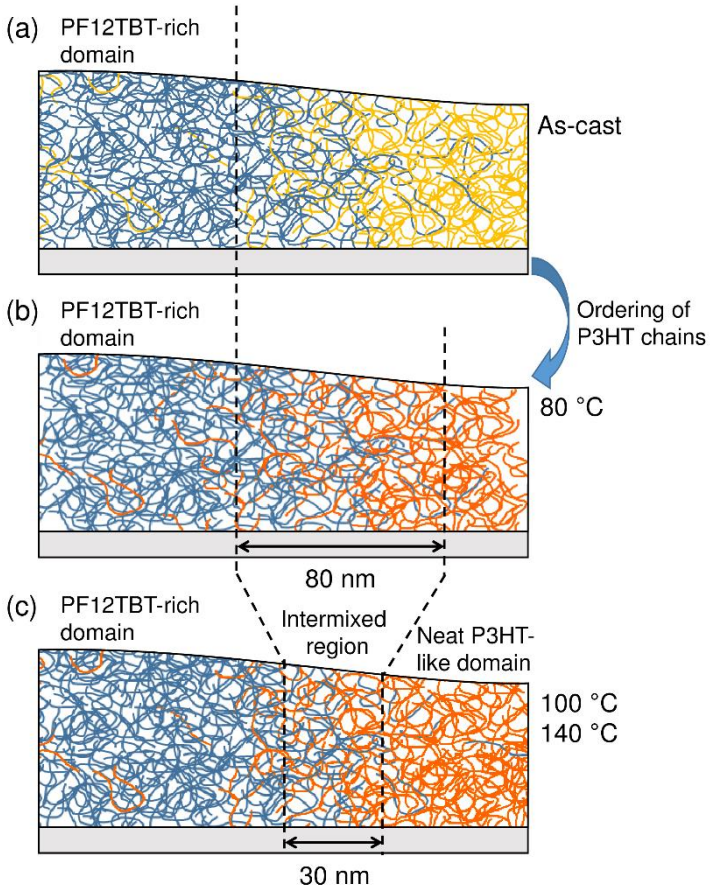

Figure 12. Schematic illustration of the intermixed region in the P3HT/PF12TBT blend films that were (a) as-cast, (b) annealed at 80 °C, and (c) annealed at 100 and 140 °C, as revealed by C-AFM hole-current images.

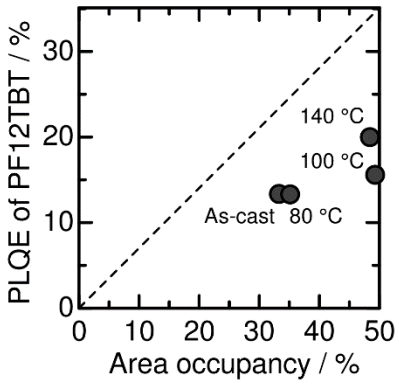

Figure 13. Plot of PLQE against the area occupancy of the PF12TBT-rich domain in each blend film (black circles). The broken line represents the expected values of PLQE under the assumption that the PL of PF12TBT was quenched in the P3HT-rich domain but not in the PF12TBT-rich domain.

Relationship between Morphology and Macroscopic Device Performance. Finally, we will show the relationship between the nanomorphology of the P3HT/PF12TBT blend films and their macroscopic device parameters. Charge carriers were generated efficiently within the intermixed region because of the large interface area between the donor and acceptor polymers.[15] After the annealing processes at temperatures up to 80 °C, the value of J_{SC} was increased from that of the as-cast blend film because the hole-transport ability in the intermixed region improved owing to the ordering of P3HT chains without enhancing the span of the phase-separation zone. This means that a larger amount of charge carriers could be transported to the electrodes, while the charge-generation efficiency remained as high as that in the as-cast blend film. On the other hand, the value of J_{SC} dropped drastically after annealing at 100 °C because the intermixed region was shrunken by the growth of the neat P3HT-like and PF12TBT-rich domains. Meanwhile, the shrinking intermixed region reduced the recombination loss of charge carriers because the holes and electrons could be transported more efficiently through the spatially separated P3HT and PF12TBT networks in each domain. Consequently, the value of FF mostly increased when the blend film was annealed at 100 °C.

CONCLUSION

Thermally induced morphological change of the donor/acceptor interface in conjugated polymer blends was revealed by electrical characterization via C-AFM measurements. In the as-cast P3HT/PF12TBT blend film, the local conductivity of the P3HT-rich domain was significantly small compared with that of the as-cast neat P3HT film because of intermixing with a considerable portion of PF12TBT as a minor component. In other words, the P3HT-rich domain in the as-cast blend mostly consisted of the intermixed region but did not contain neat P3HT-like domains. In the blend film after thermal annealing, on the other hand, neat P3HT-like domains arose in the middle of the intermixed region. Such morphological change

was triggered by the presence of the intermixed region with a composition gradient. At annealing temperatures above the glass-transition point of PF12TBT, the neat P3HT-like domains further grew in size, accompanied by decomposition of the intermixed region, leading to the formation of the donor/acceptor interface. These evolving features of the blend morphology accounted for the temperature dependencies of J_{SC} and FF of the solar cells prepared from the blend films. Our results demonstrate that electrical characterization of conjugated-polymer blends by C-AFM is critical for visualizing the morphological features that govern their device functions.

ASSOCIATED CONTENT

Supporting Information.

The Supporting Information is available free of charge via the Internet at http://pubs.acs.org. Cross-sectional topographical and current profiles, autocorrelation functions, local *I*–*V* curves, surface potential, and absorption spectra (PDF)

AUTHOR INFORMATION

Corresponding Author

*Tel. +81-743-72-6027; Fax +81-743-72-6047; e-mail benten@ms.naist.jp (H.B.)

ACKNOWLEDGMENTS

The authors thank Sumitomo Chemical Co., Ltd. for synthesizing and characterizing the acceptor polymer PF12TBT. This work was supported by the CREST program of the Japan Science and Technology Agency, JSPS KAKENHI Grant Number 26288060, and the Kansai Research Foundation for technology promotion.

REFERENCES

(1) Moos, E. Conjugated Polymer Blends: Linking Film Morphology to Performance of Light Emitting Diodes and Photodiodes. *J. Phys.: Condens. Matter* **2002**, *14*, 12235–12260.

(2) Cacialli, F.; Stoneham, M. Polymer Electronics: the Skill Lies in the Blending. *J. Phys.: Condens. Matter* **2002**, *14*, V9–V11.

(3) McNeill, C. R.; Greenham, N. C. Conjugated-Polymer Blends for Optoelectronics. *Adv. Mater*. **2009**, *21*, 3840–3850.

(4) Facchetti, A. Polymer Donor-Polymer Acceptor (All-Polymer) Solar Cells. *Mater. Today* **2013**, *16*, 123–132.

(5) Benten, H.; Mori, D.; Ohkita, H.; Ito, S. Recent Research Progress of Polymer Donor/Polymer Acceptor Blend Solar Cells. *J. Mater. Chem. A* **2016**, *4*, 5340–5365.

(6) Kang, H.; Lee, W.; Oh, J.; Kim, T.; Lee, C.; Kim, B. J. From Fullerene–Polymer to All-Polymer Solar Cells: The Importance of Molecular Packing, Orientation, and Morphology Control. *Acc. Chem. Res*. **2016**, *49*, 2424–2434.

(7) McNeill, C. R. Morphology of All-Polymer Solar Cells, *Energy Environ. Sci*. **2012**, *5*, 5653–5667.

(8) Shi, G.; Yuan, J.; Huang, X.; Lu, Y.; Liu, Z.; Peng, J.; Ding, G.; Shi, S.; Sun, J.; Lu, K.; Wang, H. -Q.; Ma, W. Combinative Effect of Additive and Thermal Annealing Processes Delivers High Efficiency All-Polymer Solar Cells. *J. Phys. Chem. C* **2015**, *119*, 25298–25306.

(9) Lee, C.; Li, Y.; Lee, W.; Lee, Y.; Choi, J.; Kim, T.; Wang, C.; Gomez, E. D.; Woo, H, Y.; Kim, B. J. Correlation between Phase-Separated Domain Sizes of Active Layer and Photovoltaic Performances in All-Polymer Solar Cells. *Macromolecules* **2016**, *49*, 5051–5058.

(10) McNeill, C. R.; Westenhoff, S.; Groves, C.; Friend, R. H.; Greenham, N. C. Influence of Nanoscale Phase Separation on the Charge Generation Dynamics and Photovoltaic Performance of Conjugated Polymer Blends: Balancing Charge Generation and Separation. *J.*

Phys. Chem. C **2007**, *111*, 19153–19160.

(11) Gu, X.; Yan, H.; Kurosawa, T.; Schroeder, B. C.; Gu, K. L.; Zhou, Y.; To, J. W. F.; Oosterhout, S. D.; Savikhin, V.; Molina-Lopez, F.; Tassone, C. J.; Mannsfeld, S. C. B.; Wang, C.; Toney, M. F.; Bao, Z. Comparison of the Morphology Development of Polymer-Fullerene and Polymer-Polymer Solar Cells during Solution-Shearing Blade Coating. *Adv. Energy. Mater*. **2016**, *6*, 1601225.

(12) Guo, Y.; Li, Y.; Awartani, O.; Zhao, J.; Han, H.; Ade, H.; Zhao, D.; Yan, H. A Vinylene-Bridged Perylenediimide-Based Polymeric Acceptor Enabling Efficient All-Polymer Solar Cells Processed under Ambient Conditions. *Adv. Mater*. **2016**, *28*, 8483–8489.

(13) Mori, D.; Benten, H.; Ohkita, H.; Ito, S. Morphology-Limited Free Carrier Generation in Donor/Acceptor Polymer Blend Solar Cells Composed of Poly(3-hexylthiophene) and Fluorene-Based Copolymer. *Adv. Energy Mater*. **2015**, *5*, 1500304.

(14) Lyons, B. P.; Clarke, N.; Groves, C. The Relative Importance of Domain Size, Domain Purity and Domain Interfaces to the Performance of Bulk-Heterojunction Organic Photovoltaics. *Energy Environ. Sci*. **2012**, *5*, 7657–7663.

(15) Snaith, H. J.; Arias, A. C.; Morteani, A. C.; Silva, C.; Friend, R. H. Charge Generation Kinetics and Transport Mechanisms in Blended Polyfluorene Photovoltaic Devices. *Nano Lett*. **2002**, *2*, 1353–1357.

(16) Pingree, L. S. C.; Reid, O. G.; Ginger, D. S. Electrical Scanning Probe Microscopy on Active Organic Electronic Devices. *Adv. Mater*. **2009**, *21*, 19–28.

(17) Groves, C.; Reid, O. G.; Ginger, D. S. Heterogeneity in Polymer Solar Cells: Local Morphology and Performance in Organic Photovoltaics Studied with Scanning Probe Microscopy. *Acc. Chem. Res*. **2010**, *43*, 612–620.

(18) Giridharagopal, R.; Cox, P. A.; Ginger, D. S. Functional Scanning Probe Imaging of Nanostructured Solar Energy Materials. *Acc. Chem. Res*. **2016**, *49*, 1769–1776.

(19) Musumeci, C.; Liscio, A.; Palermo, V.; Samorì, P. Electronic Characterization of Supramolecular Materials at the Nanoscale by Conductive Atomic Force and Kelvin Probe Force Microscopies. *Mater. Today* **2014**, *17*, 504–517.

(20) Balke, N.; Bonnell, D.; Ginger, D. S.; Kemerink, M. Scanning Probes for New Energy Materilas: Probing Local Structure and Function. *MRS Bulletin* **2012**, *37*, 633–637.

(21) Kondo, Y.; Osaka, M.; Benten, H.; Ohkita, H.; Ito, S. Electron Transport Nanostructure of Conjugated Polymer Films Visualized by Conductive Atomic Force Microscopy. *ACS Macro Lett*. **2015**, *4*, 879–885.

(22) Mori, D.; Benten, H.; Kosaka, J.; Ohkita, H.; Ito, S.; Miyake, K. Polymer/Polymer Blend Solar Cells with 2.0% Efficiency Developed by Thermal Purification of Nanoscale-Phase-Separated Morphology. *ACS Appl. Mater. Interfaces* **2011**, *3*, 2924–2927.

(23) Zhou, Y.; Fuentes-Hernandez, C.; Shim, J.; Meyer, J.; Giordano, A. J.; Li, H.; Winget, P.; Papadopoulos, T.; Cheun, H.; Kim, J.; Fenoll, M.; Dindar, A.; Haske, W.; Najafabadi, E.; Khan, T. M.; Sojoudi, H.; Barlow, S.; Graham, S.; Bredas, J.-L.; Marder, S. R.; Kahn, A. Kippelen, B. A Universal Method to Produce Low-Work Function Electrodes for Organic Electronics. *Science* **2012**, *336*, 327–332.

(24) Asadi, K.; Boer, T. G.; Blom, P. W. M.; Leeuw, D. M. Tunable Injection Barrier in Organic Resistive Switches Based on Phase-Separated Ferroelectric-Semiconductor Blends. *Adv. Funct. Mater*. **2009**, *19*, 3173–3178.

(25) Osaka, M.; Benten, H.; Lee, L.-T.; Ohkita, H.; Ito, S. Development of Highly Conductive Nanodomains in Poly(3-hexylthiophene) Film Studied by Conductive Atomic Force Microscopy. *Polymer* **2013**, *54*, 3443–3447.

(26) Osaka, M.; Benten, H.; Lee, L.-T.; Ohkita, H.; Ito, S.; Ogawa, H.; Kanaya, T. Nanostructures for Efficient Hole Transport in Poly(3-hexylthiophene) Film: A Study by Conductive Atomic Microscopy. *J. Phys. Chem. C* **2015**, *119*, 24307–24314.

(27) Suzuki, A.; Yamazaki, M.; Kobiki, Y.; Suzuki, H. Surface Domains and Roughness of Polymer Gels Observed by Atomic Force Microscopy. *Macromolecules* **1997**, *30*, 2350–2354.

(28) McNeill, C. R.; Halls, J. J. M.; Wilson, R.; Whiting, G. L.; Berkebile, S.; Ramsey, M. G.; Friend, R. H.; Greenham, N. C. Efficient Polythiophene/Polyfluorene Copolymer Bulk Heterojunction Photovoltaic Devices: Device Physics and Annealing Effects. *Adv. Funct. Mater*. **2008**, *18*, 2309–2321.

(29) McNeill, C. R.; Frohne, H.; Holdsworth, J. H.; Dastoor, P. C. Near-Field Scanning Photocurrent Measurements of Polyfluorene Blend Devices: Directly Correlating Morphology with Current Generation. *Nano Lett*. **2004**, *4*, 2503–2507.

(30) McNeill, C. R.; Watts, B.; Thomsen, L.; Belcher, W. J.; Greenham, N. C.; Dastoor, P. C.; Ade, H. Evolution of Laterally Phase-Separated Polyfluorene Blend Morphology Studied by X-ray Spectromicroscopy. *Macromolecules* **2009**, *42*, 3347–3352.

(31) McNeill, C. R.; Watts, B.; Thomsen, L.; Ade, H.; Greenham, N. C.; Dastoor, P. C. X-ray Microscopy of Photovoltaic Polyfluorene Blends: Relating Nanomorphology to Device Performance. *Macromolecules* **2007**, *40*, 3263–2370.

(32) Swaraj, S.; Wang, C.; Yan, H.; Watts, B.; Lüning, J.; McNeill, C. R.; Ade, H. Nanomorphology of Bulk Heterojunction Photovoltaic Thin Films Probed with Resonant Soft X-ray Scattering. *Nano Lett*. **2010**, *10*, 2863–2869.

(33) Walheim, S.; Böltau, M.; Mlynek, J.; Krausch, G.; Steiner, U. Structure Formation via Polymer Demixing in Spin-Cast Films. *Macromolecules* **1997**, *30*, 4995–5003.

(34) Clark, J.; Chang, J.-F.; Spano, F. C.; Friend, R. H.; Silva, C. Determining Exciton Bandwidth and Film Microstructure in Polythiophene Films Using Linear Absorption Spectroscopy. *Appl. Phys. Lett*. **2009**, *94*, 163306.

(35) Boudouris, B. W.; Ho, V.; Jimison, L. H.; Toney, M. F.; Salleo, A.; Segalman, R. A. Real-Time Observation of Poly(3-Alkylthiophene) Crystallization and Correlation with Transient

Optoelectronic Properties. *Macromolecules* **2011**, *44*, 6653–6658.

(36) Na, J. Y.; Kang, B.; Sin, D. H.; Cho, K.; Park, Y. D. Understanding Solidification of Polythiophene Thin Films during Spin-Coating: Effects of Spin-Coating Time and Processing Additives. *Sci. Rep.*, **2015**, *5*, 13288.

(37) Nishi, T.; Wang. T. T.; Kwei, T. K. Thermally Induced Phase Separation Behavior of Compatible Polymer Mixtures. *Macromolecules* **1975**, *8*, 227–234.

For Table of Contents use only

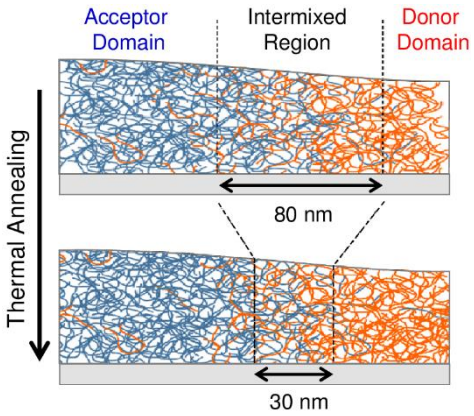

Intermixed Donor/Acceptor Region in Conjugated Polymer Blends Visualized by Conductive Atomic Force Microscopy

Miki Osaka, Hiroaki Benten, Hideo Ohkita, Shinzaburo Ito